Chaos, Solitons and Fractals 198 (2025) 116450

Contents lists available at ScienceDirect

Chaos, Solitons and Fractals

journal homepage: www.elsevier.com/locate/chaos

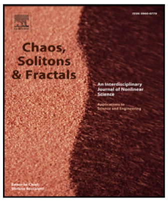

The normalized time-fractional Cahn–Hilliard equation

Hyun Geun Lee [a], Soobin Kwak [b], Seokjun Ham [b], Youngjin Hwang [b], Junseok Kim [b],*

[a] *Department of Mathematics, Dongguk University, Seoul 04620, Republic of Korea*
[b] *Department of Mathematics, Korea University, Seoul 02841, Republic of Korea*

ARTICLE INFO

Keywords:
Phase-field equation
Fourier spectral method
Phase separation
Fractional partial differential equations

ABSTRACT

We present a normalized time-fractional Cahn–Hilliard (TFCH) equation by incorporating time-fractional derivatives to model memory effects in phase separation processes. We use a normalized time-fractional derivative, which is a form of the Caputo fractional derivative, to improve the flexibility and physical interpretation of the model. This normalization allows for a more consistent interpretation of fractional orders, which enables fair comparisons across different orders of the derivative. To solve the normalized TFCH equation, we use an efficient computational scheme based on the Fourier spectral method, which ensures high accuracy and computational efficiency. Furthermore, we conduct a thorough investigation into the dynamic behavior of the normalized TFCH equation and focus on how varying the fractional-order time derivative influences the evolution and morphology of phase domains. Numerical simulations demonstrate the versatility and effectiveness of the proposed method in modeling complex phase separation dynamics.

1. Introduction

The time-fractional Cahn–Hilliard (TFCH) equation is important as it incorporates time-fractional derivatives, which allows for the modeling of memory effects and anomalous diffusion in phase separation processes. This is particularly useful for systems where the evolution depends on past states, which classical Cahn–Hilliard (CH) equations cannot capture. Real-world applications where fractional-order modeling may be relevant include digital image inpainting [1], phase separation in alloys [2], and tumor growth [3], among others. Sadaf and Akram [1] applied the time-fractional CH equation, which uses the nonlocal properties of fractional derivatives to provide a more flexible framework for applications such as digital image inpainting, where it aids in restoring degraded text and high-contrast images. Zhao et al. [2] observed that the energy follows a scaling behavior of approximately $O(t^{-\frac{\alpha}{3}})$, which is consistent with the scaling $O(t^{-\frac{1}{3}})$ observed for the integer-order CH equation with constant mobility. This result indicates that the exponent in the power-law scaling is linearly dependent on the fractional order α.

The classical CH equation was originally derived to describe spinodal decomposition, as detailed in the works of Cahn and Hilliard [4,5]. Extensions of the CH equation have enabled applications in multi-component systems, as shown in studies involving advanced discretization methods for multi-component CH systems [6]. Yang et al. [7] presented a temporally second-order, linearly implicit-explicit, and energy-stable scheme for the ternary CH system coupled with NS equations based on the scalar auxiliary variable method. Furthermore, the CH equation has been extensively adapted to represent a variety of other physical processes [8]. In the study of liquid–liquid jets, energy-stable schemes and phase-field methods were developed to simulate multi-phase dynamics [9]. Multi-phase modeling includes simulations of compound droplets on solid surfaces [10] and binary thermal fluids on arbitrary surfaces [11]. In the field of crystal growth, the CH equation was applied to study nucleation and crystalline transitions through the Lagrange multiplier framework [12]. It was also used for modeling anisotropic dendritic growth with orientation fields, which provides robust numerical methods for complex morphologies [13]. Recent developments integrated the CH-based models with the Swift–Hohenberg equation for curved surfaces [14]. The CH equation was also applied in topology optimization, such as designing shell-infill structures using phase-field-based methods [15]. It was further used in thermal-fluid topology optimization for systems [16] and adapted for analyzing biological transport networks in complex domains [17]. In surface and volume reconstruction, it was extended to applications like multi-component volume reconstruction from slice data, which provides practical solutions for imaging and pattern recognition tasks [18]. Li and Yang [19] developed a novel diffuse interface model for the CH equation, which improves local volume conservation and accurately simulating Rayleigh–Plateau instability coupled with incompressible Navier–Stokes (NS) equations.

---

* Corresponding author.
E-mail address: cfdkim@korea.ac.kr (J. Kim).
URL: https://mathematicians.korea.ac.kr/cfdkim (J. Kim).

https://doi.org/10.1016/j.chaos.2025.116450
Received 16 December 2024; Received in revised form 16 March 2025; Accepted 11 April 2025

Zheng and Jiang [20] developed the L1 Fourier spectral method by applying the Fourier spectral method in space and the L1 finite difference method to discretize the Caputo time-fractional derivative to solve the time-fractional NS equation with periodic boundary conditions. The authors conducted an analysis of the stability and convergence of the developed computational scheme and performed numerical simulations to verify its effectiveness.

Meanwhile, the TFCH equation, which accounts for nonlocal and history-dependent behavior, offered broader applications and more accurate phase evolution simulations, particularly for non-equilibrium systems.

Nonlocal effects inherently arise in time-fractional partial differential equations (PDEs), which have widespread uses owing to inherent memory effects [21]. These include areas such as signal processing [22], plasticity [23], image processing [24], viscoelasticity [25–27], and the mechanical properties of materials [28].

Fractional nonlocal elasticity models have also been used in the bending analysis of functionally graded nanobeams, where fractional operators effectively capture small-scale effects [29]. Sumelka et al. [30] proposed the Fractional Euler–Bernoulli beam theory by reformulating the classical Euler–Bernoulli beam theory using fractional calculus and conducted a numerical study and experimental validation. Lazopoulos and Lazopoulos [31] proposed a theory on the fractional bending of a beam using the Euler–Bernoulli bending principle. The authors introduced a fractional tangent space and analyzed the bending of a cantilever beam under distributed loading. Lazopoulos and Lazopoulos [32] proposed new fractional derivatives satisfying differential topology and introduced the Λ-space for localization. The authors discussed fractional axial stress and elastic bar deformation using these derivatives. Sidhardh et al. [33] formulated the analytical and finite element framework for a geometrically nonlinear fractional-order nonlocal Euler–Bernoulli beam model and examined its behavior under different loading and boundary conditions. Stempin and Sumelka [34] improved the space-fractional Euler–Bernoulli beam theory by introducing new kinematics and a variable length scale. Furthermore, the authors developed a numerical algorithm to solve the bending problem.

Liu et al. [35] investigated time-fractional Allen–Cahn (AC) and CH phase-field equations to study subdiffusive transport and memory effects in materials, developed efficient numerical schemes to handle the computational challenges, and observed distinct energy decay behaviors for the two models based on the fractional order. Tang et al. [36] first validated that time-fractional phase-field equations satisfy an energy dissipation principle. Furthermore, they proposed finite difference methods for various phase-field equations such as the TFCH equation. Saleh et al. [37] applied the singular manifold method to derive exact solutions for nonlinear fractional PDEs. The authors employed this approach to solve the nonlinear TFCH equation and obtain its exact solutions. Ye et al. [38] investigated Cauchy problem for the Caputo-type TFCH equation in $\mathbb{R}^3$. The authors provided an analytic investigation of the TFCH equation, as well as its consistency with the mass conservation property of the traditional CH equation. Liao et al. [39] constructed a discrete gradient structure for the TFCH equation. Zhang et al. [40] presented an adaptive method for the TFCH equation, and provided theoretical proofs and numerical results validating its effectiveness and revealing insights into phase separation dynamics. Liu et al. [41] introduced two linear algorithms for the time-fractional CH and AC models, and performed 2D and 3D numerical simulations. Ran and Zhou [42] presented an efficient finite difference scheme for TFCH equations, using the L_1 formula for the Caputo derivative, proving stability and convergence in the discrete L_2-norm, and demonstrating through numerical experiments that the solution approaches equilibrium over time, consistent with phase separation phenomena. Sadaf and Akram [1] investigated the effects of fractional order derivatives on the numerical solutions of the TFCH equation using a modified homotopy analysis, and demonstrated the accuracy and reliability of the results through numerical and graphical illustrations. In [43], the authors investigated the front motion of the TFCH equation with two different types of diffusion mobilities and derive the corresponding sharp interface models. As a result, they demonstrated that the TFCH equation could be used to model the coarsening process. Chen and Shujuan [44] investigated the numerical approximation of the TFCH equation and proved solvability, stability, and convergence of the solution. Furthermore, they validated the theoretical results through a numerical example. Huang et al. [45] developed a fully discrete semi-implicit stabilized method for the TFCH equation, and demonstrated unconditional optimal error estimates, energy dissipation preservation, and validated theoretical convergence through numerical experiments.

Zhang and Jiang [46] developed a second-order numerical method based on the fractional backward difference formula for time-fractional phase field models, including the AC equation, the CH equation, and the time-fractional molecular beam epitaxy model. This developed method incorporates the extended scalar auxiliary variable scheme to handle the nonlinear terms. Furthermore, the authors proved the energy dissipation property. Quan et al. [47] extended the classical energy definition of phase-field equations by introducing a time-dependent weight function to average the classical energy, defining a nonlocal energy that satisfies the energy dissipation law for time-fractional phase-field models. Furthermore, in [48], the authors established two discrete energy laws, namely the time-fractional energy law and the weighted energy dissipation law. These laws were derived for three types of L1 schemes, which include the convex-splitting, the stabilization, and the scalar auxiliary variable schemes for time-fractional phase-field equations. Quan and Wang [49] analyzed the energy stability of high-order L2-type methods for time-fractional phase-field equations and proved that the energy in the L2 scalar auxiliary variable method for time-fractional gradient flows is bounded by the initial energy.

Yu et al. [50] presented time-fractional phase-field equations such as the AC and CH equations using the exponential scalar auxiliary variable algorithm, which ensures energy dissipation on nonuniform meshes.

Karaa [51] established general criteria ensuring the positivity of quadratic forms of convolution type and applied them in numerical approximations of fractional integral and differential operators. The results provide a fundamental basis for analyzing the numerical stability of time-fractional phase-field models. Without relying on a fractional Grönwall inequality, the study demonstrated that several computational methods satisfy discrete energy dissipation laws through standard energy stability analysis.

Al-Maskari and Karaa [52] investigated the regularity of the solution and derived error estimates of optimal order and proved the discrete energy dissipation characteristic of the proposed algorithm. In [53], the authors developed an efficient two-stage finite point-set scheme to solve the TFCH equation. Liang et al. [54] presented a lattice Boltzmann scheme for solving the TFCH equation. The proposed method transforms the TFCH equation into its standard form using the Caputo derivative. Khristenko and Wohlmuth [55] proposed a computational scheme for fractional differential equations based on the adaptive Antoulas–Anderson scheme. They applied this method to the TFCH equation. Qi et al. [56] developed two second-order computational methods with variable temporal steps for the TFCH model. Zhang and Liao [57] proposed second-order stable computational methods for the TFCH model. Kawarkhe et al. [58] discussed the reduced differential transform method and used this approach to obtain and analyze analytical approximate solutions for the one-dimensional homogeneous TFCH equation. In [59], the authors investigated the approximate solutions obtained by solving the TFCH equation using the least squares algorithm.

The main purpose of this article is to present the following normalized TFCH equation in two-dimensional (2D) space, which is based on a normalized time-fractional derivative [60–62]:

$$\frac{\partial^\alpha \phi(\mathbf{x},t)}{\partial t^\alpha} = \Delta[F'(\phi(\mathbf{x},t)) - \epsilon^2 \Delta\phi(\mathbf{x},t)], \quad \text{for } (\mathbf{x},t) \in \Omega \times (0,\ T), \tag{1}$$

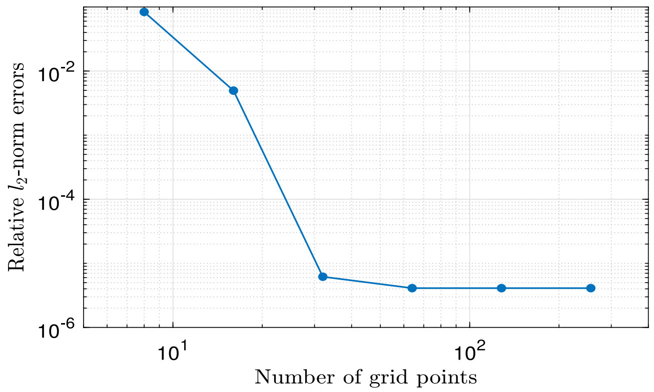

Fig. 1. Exponentially decreasing spatial errors.

where $F(\phi) = 0.25(\phi^2-1)^2$ and

$$\frac{\partial^\alpha \phi(\mathbf{x},t)}{\partial t^\alpha} = \frac{1-\alpha}{t^{1-\alpha}}\int_0^t \frac{\partial \phi(\mathbf{x},s)}{\partial s}\frac{ds}{(t-s)^\alpha}, \quad 0 \le \alpha < 1, \tag{2}$$

where the following identity is satisfied for any α and t:

$$\frac{1-\alpha}{t^{1-\alpha}}\int_0^t \frac{ds}{(t-s)^\alpha} = 1, \quad 0 \le \alpha < 1. \tag{3}$$

The normalized time-fractional derivative is not necessarily superior in all aspects compared to other definitions of fractional derivatives such as the classical Caputo, Riemann–Liouville [63], Atangana–Baleanu–Caputo [64] formulations. However, one of the key merits of the normalized time-fractional derivative is that it allows a fair comparison between different fractional orders. This normalization ensures that variations in the fractional order directly reflect changes in the physical behavior of the system, rather than being influenced by scaling artifacts. As a result, researchers can compare the effects of fractional orders on system dynamics in a consistent and meaningful way, which makes it easier to evaluate the impact of fractional behavior across different fractional order values. This property is particularly valuable for studying systems where fractional order plays a crucial role in phenomena such as subdiffusion, memory effects, and anomalous transport, which ensures that the comparisons are both rigorous and insightful.

The organization of this article is as follows. Section 2 introduces the computational algorithm for the normalized TFCH equation. Section 3 presents numerical experiments to validate the proposed approach. Lastly, Section 4 provides conclusions.

2. Numerical solutions

Let $\Omega = (L_x,\ R_x)\times(L_y,\ R_y)$ be the numerical domain and be discretized as $\Omega_h = \{(x_m,y_n)|x_m = L_x+(m-0.5)h,\ 1\le m\le N_x$ and $y_n = L_y+(n-0.5)h,\ 1\le n\le N_y\}$, where $h=(R_x-L_x)/N_x$ for some positive integer N_x. Let $\phi_{mn}^k = \phi\left(x_m,y_n,t_k\right)$ and $t_k=(k-1)\Delta t$. Then, we have

$$\begin{aligned}\frac{\partial^\alpha \phi(x_m,y_n,t_{k+1})}{\partial t^\alpha} &= \frac{1-\alpha}{t_{k+1}^{1-\alpha}}\sum_{r=1}^{k}\int_{t_r}^{t_{r+1}}\frac{\partial\phi(x_m,y_n,s)}{\partial s}\frac{ds}{(t_{k+1}-s)^\alpha} \\ &\approx \sum_{r=1}^{k}\frac{1-\alpha}{t_{k+1}^{1-\alpha}}\int_{t_r}^{t_{r+1}}\frac{ds}{(t_{k+1}-s)^\alpha}\frac{\phi_{mn}^{r+1}-\phi_{mn}^{r}}{\Delta t} \\ &= \sum_{r=1}^{k}\frac{(n+1-r)^{1-\alpha}-(n-r)^{1-\alpha}}{n^{1-\alpha}}\frac{\phi_{mn}^{r+1}-\phi_{mn}^{r}}{\Delta t} \\ &= \sum_{r=1}^{k} w_r^k\frac{\phi_{mn}^{r+1}-\phi_{mn}^{r}}{\Delta t} \\ &= w_n^k\frac{\phi_{mn}^{k+1}-\phi_{mn}^{k}}{\Delta t}+\sum_{r=1}^{k-1} w_r^k\frac{\phi_{mn}^{r+1}-\phi_{mn}^{r}}{\Delta t},\end{aligned} \tag{4}$$

where $w_r^k = [(k+1-r)^{1-\alpha}-(k-r)^{1-\alpha}]/k^{1-\alpha}$, which satisfies $\sum_{r=1}^{k} w_r^k = 1$.

For the sake of completeness in presenting the numerical solution algorithm using the Fourier spectral method, we briefly outline the procedure here. Further details can be found in [35,65]. Let $\{\phi_{mn}^k|1\le m\le N_x$ and $1\le n\le N_y\}$ be the given data, and define the discrete Fourier transform as follows:

$$\hat{\phi}_{pq}^k = \sum_{m=1}^{N_x}\sum_{n=1}^{N_y}\phi_{mn}^k e^{-i(\xi_p x_m+\eta_q y_n)}, \quad -\frac{N_x}{2}+1\le p\le\frac{N_x}{2},\ -\frac{N_y}{2}+1\le q\le\frac{N_y}{2}, \tag{5}$$

where $\xi_p = 2\pi p/L_x$ and $\eta_q = 2\pi q/L_y$. Then, the inverse discrete Fourier transform can be defined as follows:

$$\phi_{mn}^k = \frac{1}{N_xN_y}\sum_{p=-N_x/2+1}^{N_x/2}\ \sum_{q=-N_y/2+1}^{N_y/2}\hat{\phi}_{pq}^k e^{i(\xi_p x_m+\eta_q y_n)}. \tag{6}$$

$$\begin{aligned}\frac{\partial}{\partial x}\phi(x,y,t) &= \frac{1}{N_xN_y}\sum_{p=-N_x/2+1}^{N_x/2}\ \sum_{q=-N_y/2+1}^{N_y/2}(i\xi_p)\hat{\phi}(\xi_p,\eta_q,t)e^{i(\xi_p x+\eta_q y)}, \\ \frac{\partial}{\partial y}\phi(x,y,t) &= \frac{1}{N_xN_y}\sum_{p=-N_x/2+1}^{N_x/2}\ \sum_{q=-N_y/2+1}^{N_y/2}(i\eta_q)\hat{\phi}(\xi_p,\eta_q,t)e^{i(\xi_p x+\eta_q y)},\end{aligned} \tag{7}$$

where $\phi(x,y,t)$ is a continuous extension of ϕ_{mn}^k. Then, we can obtain

$$\begin{aligned}\Delta\phi(x,y,t) &= \frac{1}{N_xN_y}\sum_{p=-N_x/2+1}^{N_x/2}\ \sum_{q=-N_y/2+1}^{N_y/2}\widehat{\Delta\phi}(\xi_p,\eta_q,t)e^{i(\xi_p x+\eta_q y)} \\ &= \frac{1}{N_xN_y}\sum_{p=-N_x/2+1}^{N_x/2}\ \sum_{q=-N_y/2+1}^{N_y/2}-(\xi_p^2+\eta_q^2)\hat{\phi}(\xi_p,\eta_q,t)e^{i(\xi_p x+\eta_q y)}.\end{aligned} \tag{8}$$

Then, we get the computational solution of the normalized TFCH equation. We use the well-known linearly stabilized splitting method [66] to Eq. (1).

$$w_k^k\frac{\phi_{mn}^{k+1}-\phi_{mn}^k}{\Delta t} = [\Delta\left(2\phi_{mn}^{k+1}-\epsilon^2(\Delta\phi^{k+1})_{mn}+f(\phi_{mn}^k)\right)]_{mn}-s_{mn}^k, \tag{9}$$

where $f(\phi)=\phi^3-3\phi$ and $s_{mn}^k = \sum_{r=1}^{k-1}w_r^k(\phi_{mn}^{r+1}-\phi_{mn}^r)/\Delta t$. Thus, we transform Eq. (9) into the following form:

$$w_k^k\frac{\hat{\phi}_{pq}^{k+1}-\hat{\phi}_{pq}^k}{\Delta t} = -\left(\xi_p^2+\eta_q^2\right)\left(2\hat{\phi}_{pq}^{k+1}+\epsilon^2(\xi_p^2+\eta_q^2)\hat{\phi}_{pq}^{k+1}+\hat{f}_{pq}^k\right)-\hat{s}_{pq}^k, \tag{10}$$

which is rewritten as

$$\hat{\phi}_{pq}^{k+1} = \frac{w_k^k\hat{\phi}_{pq}^k-(\xi_p^2+\eta_q^2)\Delta t\hat{f}_{pq}^k-\Delta t\hat{s}_{pq}^k}{w_k^k+\Delta t[2(\xi_p^2+\eta_q^2)+\epsilon^2(\xi_p^2+\eta_q^2)^2]}. \tag{11}$$

Finally, we have ϕ_{mn}^{k+1} using Eq. (6) as follows:

$$\phi_{mn}^{k+1} = \frac{1}{N_xN_y}\sum_{p=-N_x/2+1}^{N_x/2}\ \sum_{q=-N_y/2+1}^{N_y/2}\hat{\phi}_{pq}^{k+1}e^{i(\xi_p x_m+\eta_q y_n)}. \tag{12}$$

3. Computational tests

To verify the convergence of the numerical method used, the initial condition is considered:

$$\phi(x,y,0) = 0.25\sin(2\pi x)\cos(2\pi y), \qquad (x,y)\in\Omega,$$

where $\Omega=(0,1)\times(0,1)$. For the convergence test, we commonly set $\epsilon=0.05$, and $T=0.2$. The relative l_2-norm error is defined as follows:

$$E(h,\Delta t) = \frac{\|\phi^n-\phi_{ref}^n\|_2}{\|\phi^n\|_2},$$

where ϕ_{ref} denotes the reference solution, and $\|\phi^n\|_2 = \sqrt{1/(N_xN_y)\sum_{j=1}^{N_y}\sum_{i=1}^{N_x}(\phi_{ij}^n)^2}$. The temporal error is investigated by progressively halving the time step size as $\Delta t = 0.2/2^5,\ 0.2/2^6,\ 0.2/2^7,$

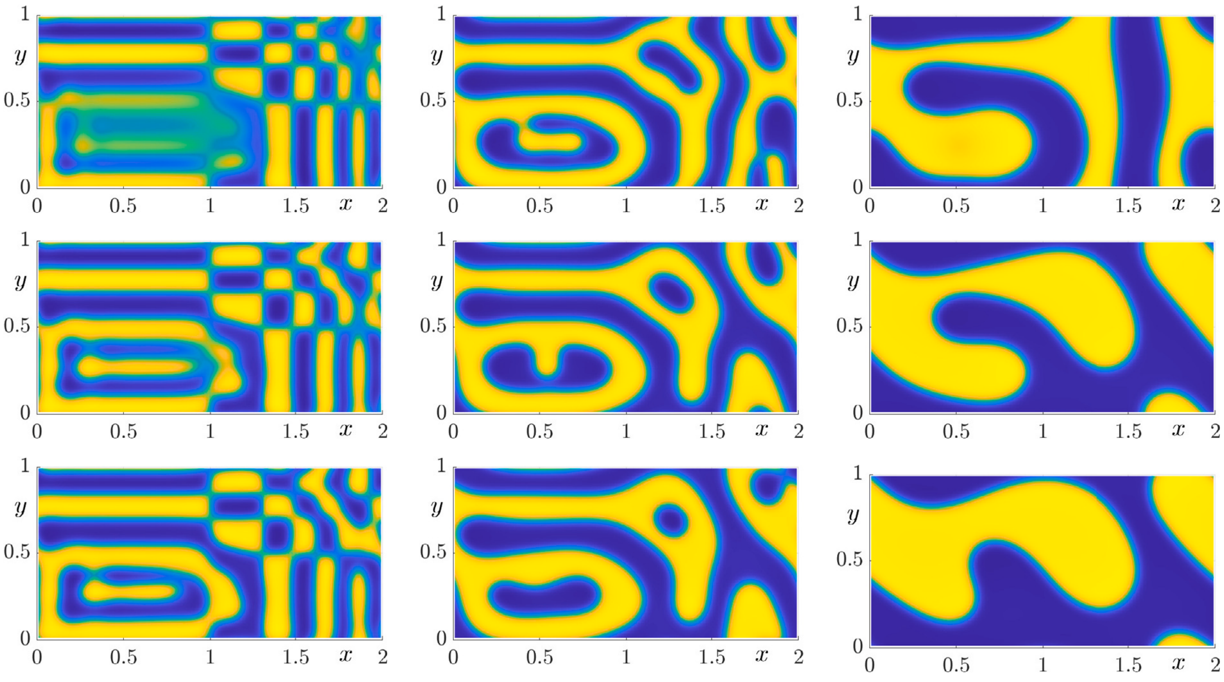

(a) (b) (c)

Fig. 2. (a), (b), and (c) are the numerical results for the normalized TFCH equation at times $t = 40\Delta t$, $200\Delta t$, and $1240\Delta t$, respectively. The solutions are arranged in rows, with the top, middle, and bottom rows corresponding to $\alpha = 1$, $\alpha = 0.5$, and $\alpha = 0.1$, respectively.

Table 1
The temporal errors and convergence rates.

Δt	$0.2/2^5$	Rate	$0.2/2^6$	Rate	$0.2/2^7$	Rate	$0.2/2^8$
l_2-error	2.4969e−3	1.33	9.9291e−4	1.14	4.5001e−4	1.10	2.0963e−4

and $0.2/2^8$. The number of grid points is fixed at 256, and ϕ_{ref} is obtained using $\Delta t = 0.2/2^{12}$. Table 1 provides the temporal errors and convergence rates for each time step size.

We investigate the spatial error and use $\Delta t = 0.2/2^8$, which provides sufficient accuracy in time. The spatial error is computed for the number of grid points $N_x \times N_y = 2^N \times 2^N$ with $N = 3, 4, \ldots, 8$, and ϕ_{ref} is obtained using $2^{11} \times 2^{11}$. Fig. 1 shows that the spatial error decreases exponentially.

We perform a set of computational tests to validate the performance of the proposed normalized TFCH equation and investigate its dynamic behavior under various conditions. The computational tests focus on the influence of the fractional order parameter α on evolutions. Let us take into account the following initial profile defined within $\Omega = (0,\ 2) \times (0,\ 1)$:

$$\phi(\mathbf{x}, 0) = 0.05\cos(0.5\pi x^4)\cos(4\pi y^3). \tag{13}$$

We use $N_x = 100$, $N_y = 50$, $\epsilon = h$, and $\Delta = h^2$. Fig. 2(a), (b), and (c) illustrate the numerical solutions of the normalized TFCH equation at various times $t = 40\Delta t$, $200\Delta t$, and $1240\Delta t$, respectively, for various values of the fractional order α. Each column demonstrates how the system evolves over time. The rows correspond to various values of α, with the top row for $\alpha = 1$, the middle row for $\alpha = 0.5$, and the bottom row for $\alpha = 0.1$. The evolution of the phase separation process varies with α. For $\alpha = 1$, which represents the classical CH equation, the system evolves more slowly toward equilibrium. As α decreases (0.5 and 0.1), the dynamics becomes faster, indicating that the memory effects introduced by the time-fractional derivative lead to a faster phase separation process. This shows how α influences the rate and nature of phase evolution in the system, with smaller α values yielding faster transitions.

Then, we consider a square spiral as an initial condition as shown in the first column of Fig. 3 with $\alpha = 1$ and $\alpha = 0.1$. We use $N_x = 100$, $N_y = 100$, $h = 1/100$, $\epsilon = h$, and $\Delta t = h^2$ on $\Omega = (0, 1) \times (0, 1)$. Fig. 3 illustrates the time evolution of the computational solutions for two values of α: (a) $\alpha = 1$ and (b) $\alpha = 0.1$. The evolution progresses faster as α decreases.

To compare the numerical results of the classical Caputo derivative and the proposed normalized model, we consider the following initial condition for the CH equation, which leads to growth and phase separation.

$$\phi(x, y, 0) = 0.1\cos\left(\frac{\pi}{50}x\right)\cos\left(\frac{\pi}{50}y\right), \quad (x, y) \in (0, 100) \times (0, 100).$$

A large-scale domain is used to observe the effects of the fractional order over time. We use the parameters as $h = 1$, $\Delta t = 1$, and $\epsilon = h$ for the numerical tests. Fig. 4 illustrates the temporal evolution of the solution for two different fractional derivative formulations applied to the CH equation with fractional order $\alpha = 0.9$: (a) the classical Caputo fractional derivative and (b) the normalized fractional derivative. The evolution is presented at three distinct time steps, $t = 60\Delta t$, $84\Delta t$, and $120\Delta t$. For the fractional order of $\alpha = 0.9$, the solution obtained using the normalized fractional derivative exhibits faster separation compared to the results obtained with the Caputo derivative.

Fig. 5 illustrates the temporal evolution of the solution for two different fractional derivative formulations applied to the CH equation: (a) the classical Caputo fractional derivative and (b) the normalized fractional derivative. The evolution is presented at three distinct time steps, $t = 40\Delta t$, $64\Delta t$, and $80\Delta t$. In the case of the normalized fractional derivative, the evolution is significantly faster for $\alpha = 0.1$ compared to $\alpha = 0.9$. In contrast, for the classical Caputo derivative, the solution becomes pinned, exhibiting no further evolution.

Next, we investigate the temporal evolution of two droplets in contact with the following initial condition:

$$\phi(x, y, 0) = \begin{cases} 1, & \text{if } (x+1)^2 + y^2 \le 1 \text{ or } (x-1)^2 + y^2 \le 1, \\ -1, & \text{otherwise,} \end{cases}$$

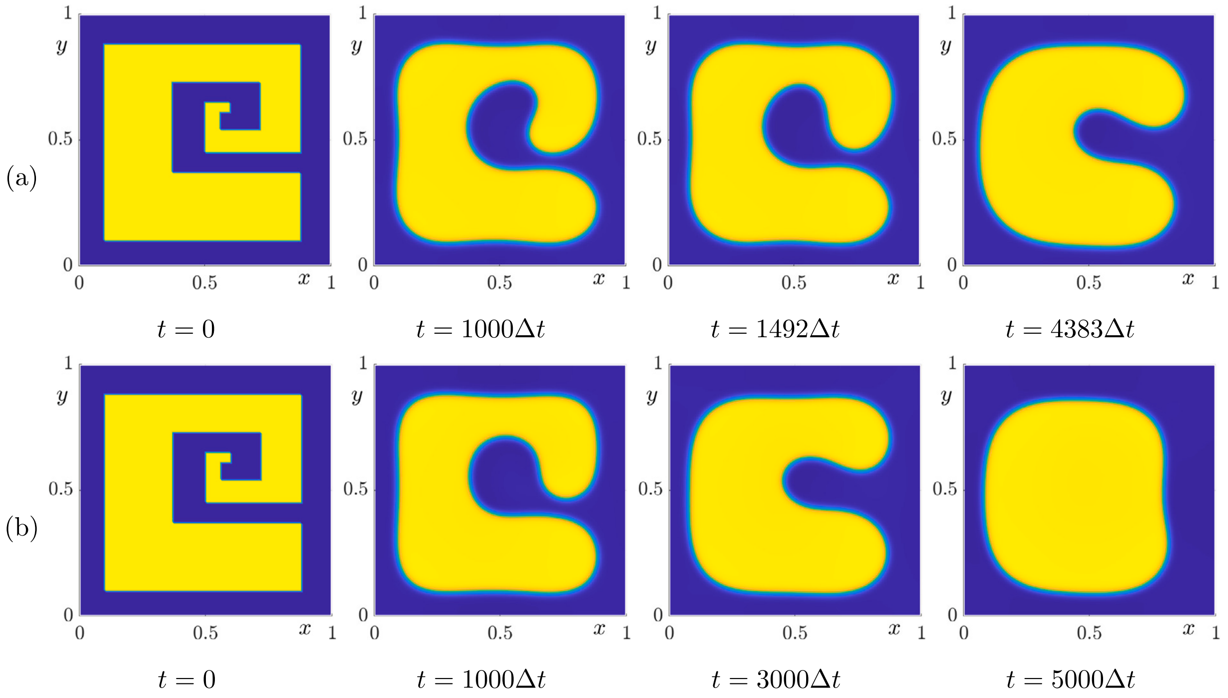

Fig. 3. Time evolutions of the computational results for (a) $\alpha = 1$ and (b) $\alpha = 0.1$. The time is indicated below each figure.

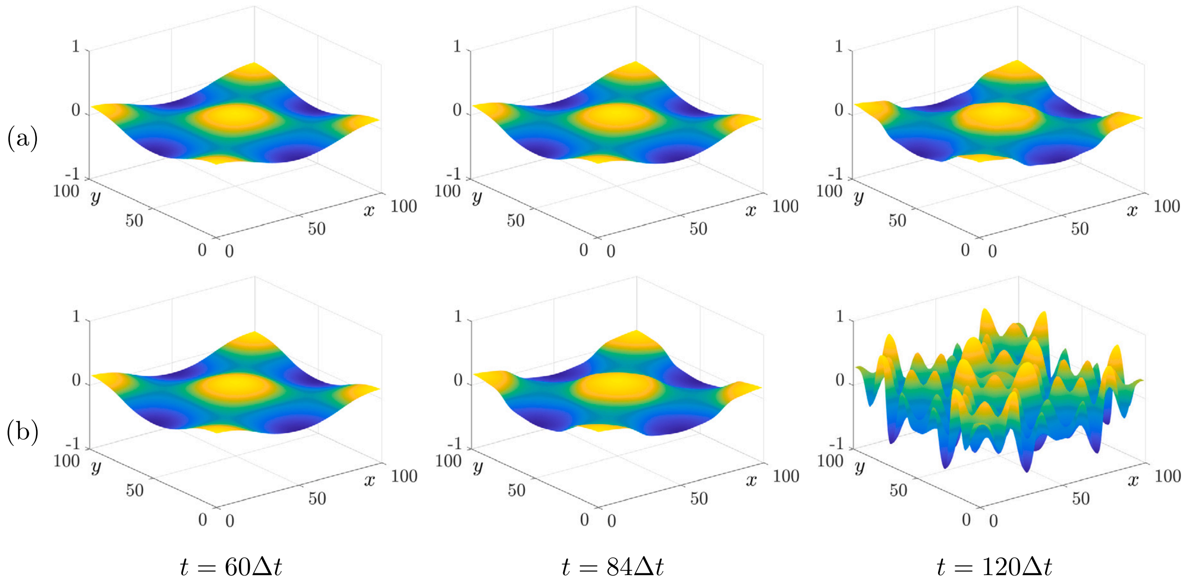

Fig. 4. Temporal evolution of the solution for (a) the classical Caputo fractional derivative and (b) the normalized fractional derivative applied to the CH equation with fractional order $\alpha = 0.9$. The columns correspond to different time steps, $t = 60\Delta t$, $84\Delta t$, and $120\Delta t$.

on a computational domain $\Omega = (-\pi, \pi) \times (-\pi, \pi)$. $N_x = N_y = 128$, $\Delta t = 0.01$, and $\epsilon = 0.1$ are used. Fig. 6 displays the temporal evolution of the two droplets with four different values of $\alpha = 0$, 0.1, 0.5, and 1. In Fig. 6, the snapshots, from the left column, are taken at $t = 0$, $100\Delta t$, $1000\Delta t$, $4000\Delta t$. When the value of α decreases, the merging process leading to a single circular droplet is delayed.

Next, we consider the deformation of a droplet under the influence of a specified background flow, which is defined by swirling velocity fields that introduce complex advective effects on the droplet's evolution. We consider the following governing equation with an advection term:

$$\frac{\partial^\alpha \phi(\mathbf{x},t)}{\partial t^\alpha} + \nabla\cdot\big(\phi(\mathbf{x},t)\mathbf{u}(\mathbf{x},t)\big) = \Delta[F'(\phi(\mathbf{x},t)) - \epsilon^2\Delta\phi(\mathbf{x},t)], \tag{14}$$

where $\mathbf{u}(\mathbf{x},t)$ is the background flow. Here, the convection term in Eq. (14) is numerically solved by the conservative finite difference method:

$$\nabla_h\cdot\left(\phi_{ij}^n\mathbf{u}_{ij}^n\right) = \frac{(\phi_{i+1,j}^n+\phi_{ij}^n)u_{i+\frac{1}{2},j}^n - (\phi_{ij}^n+\phi_{i-1,j}^n)u_{i-\frac{1}{2},j}^n}{2h} + \frac{(\phi_{i,j+1}^n+\phi_{ij}^n)u_{i,j+\frac{1}{2}}^n - (\phi_{ij}^n+\phi_{i,j-1}^n)u_{i,j-\frac{1}{2}}^n}{2h}.$$

First, we consider the background swirling flow $\mathbf{u}(\mathbf{x},t) = (u(\mathbf{x},t), v(\mathbf{x},t))$ defined as

$$u(\mathbf{x},t) = -2.5\sin^2(\pi x)\sin(2\pi y) \quad\text{and}\quad v(\mathbf{x},t) = 2.5\sin^2(\pi y)\sin(2\pi x).$$

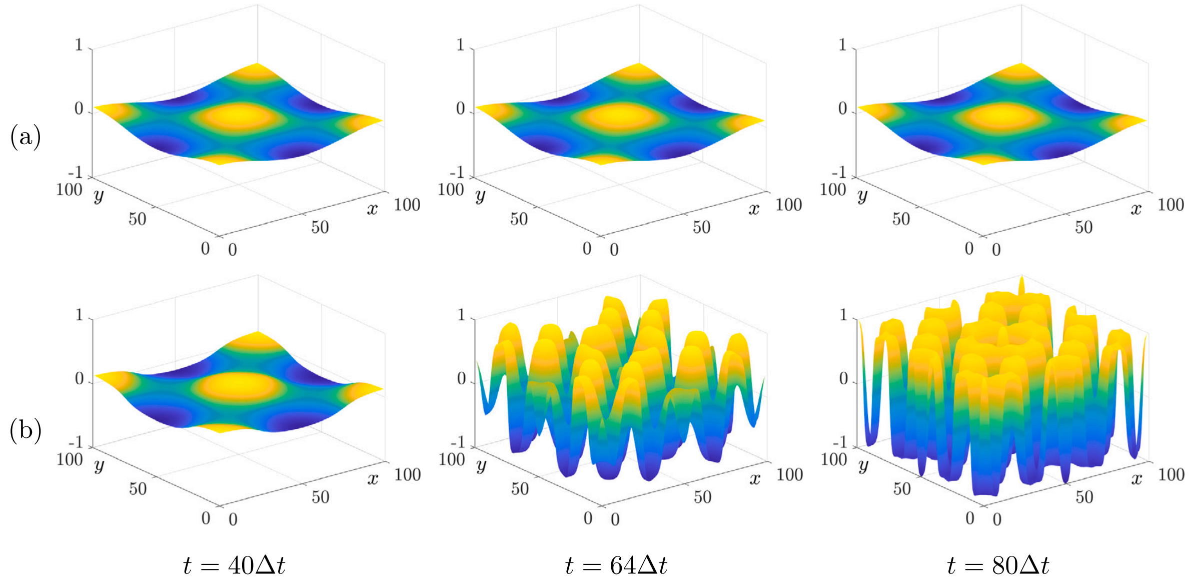

Fig. 5. Temporal evolution of the solution for (a) the classical Caputo fractional derivative and (b) the normalized fractional derivative applied to the CH equation with fractional order $\alpha = 0.1$. The columns correspond to different time steps, $t = 40\Delta t$, $64\Delta t$, and $80\Delta t$.

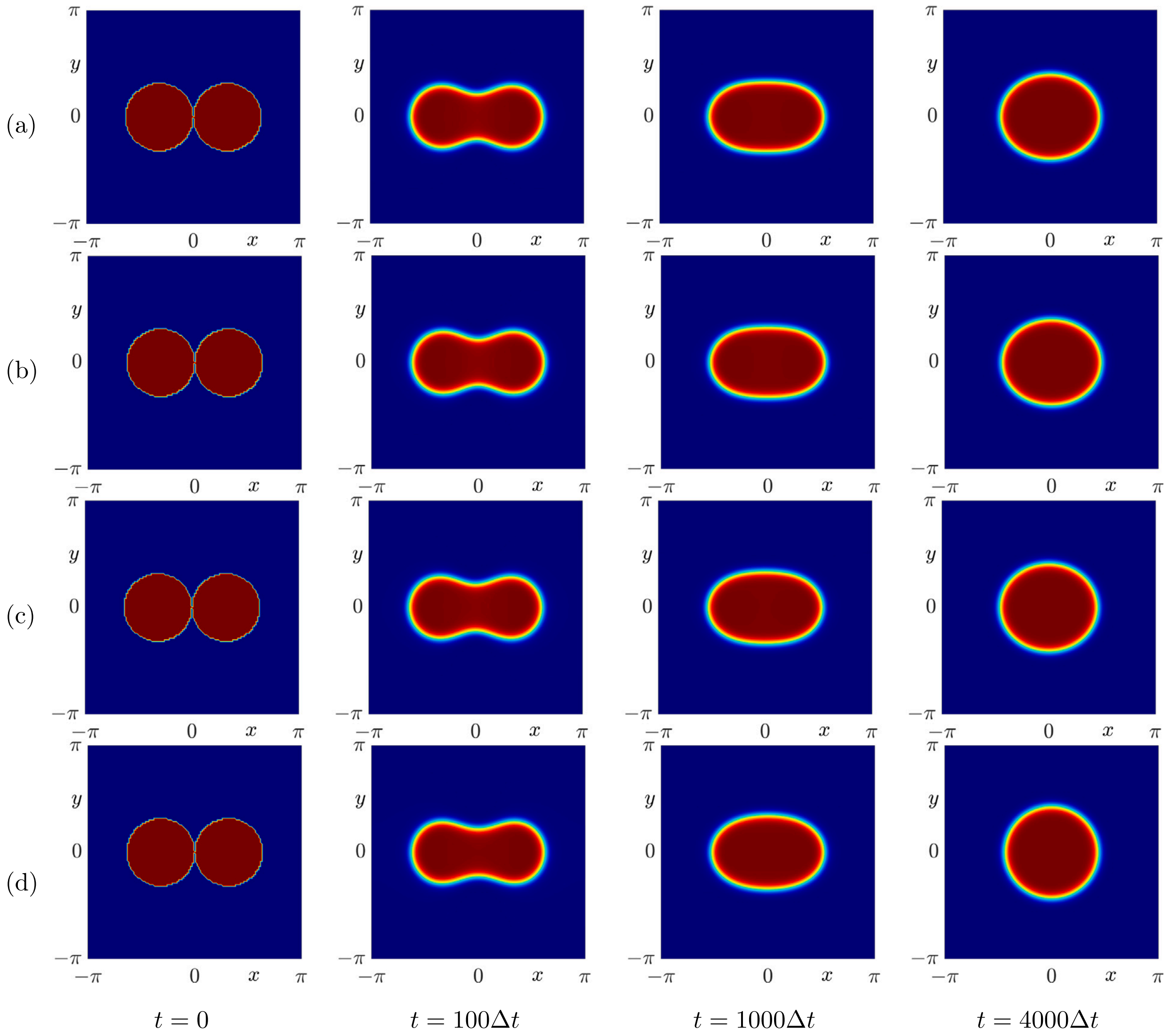

Fig. 6. Temporal evolution of two droplets with (a) $\alpha = 0$, (b) $\alpha = 0.1$, (c) $\alpha = 0.5$, and (d) $\alpha = 1$.

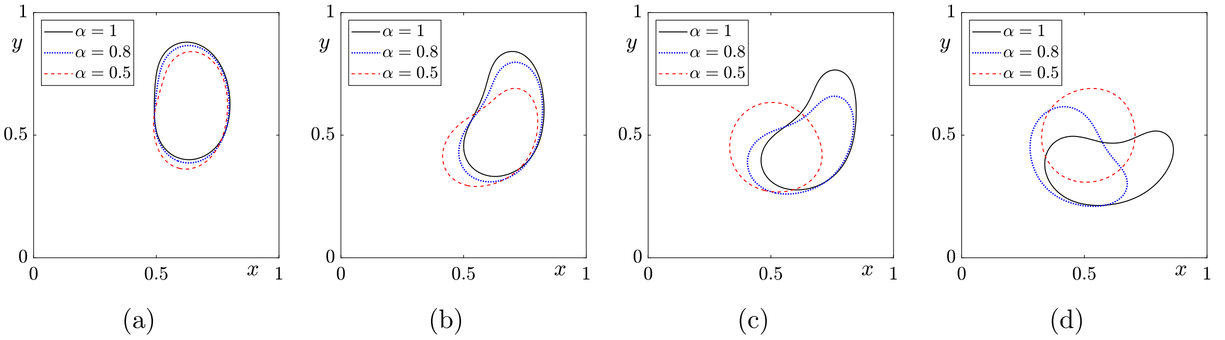

Fig. 7. Time evolution of the zero-level set of the computational solutions for $\alpha = 1$, $\alpha = 0.8$, and $\alpha = 0.5$ at (a) $t = 1000\Delta t$, (b) $t = 1500\Delta t$, (c) $t = 2000\Delta t$, and (d) $t = 3000\Delta t$.

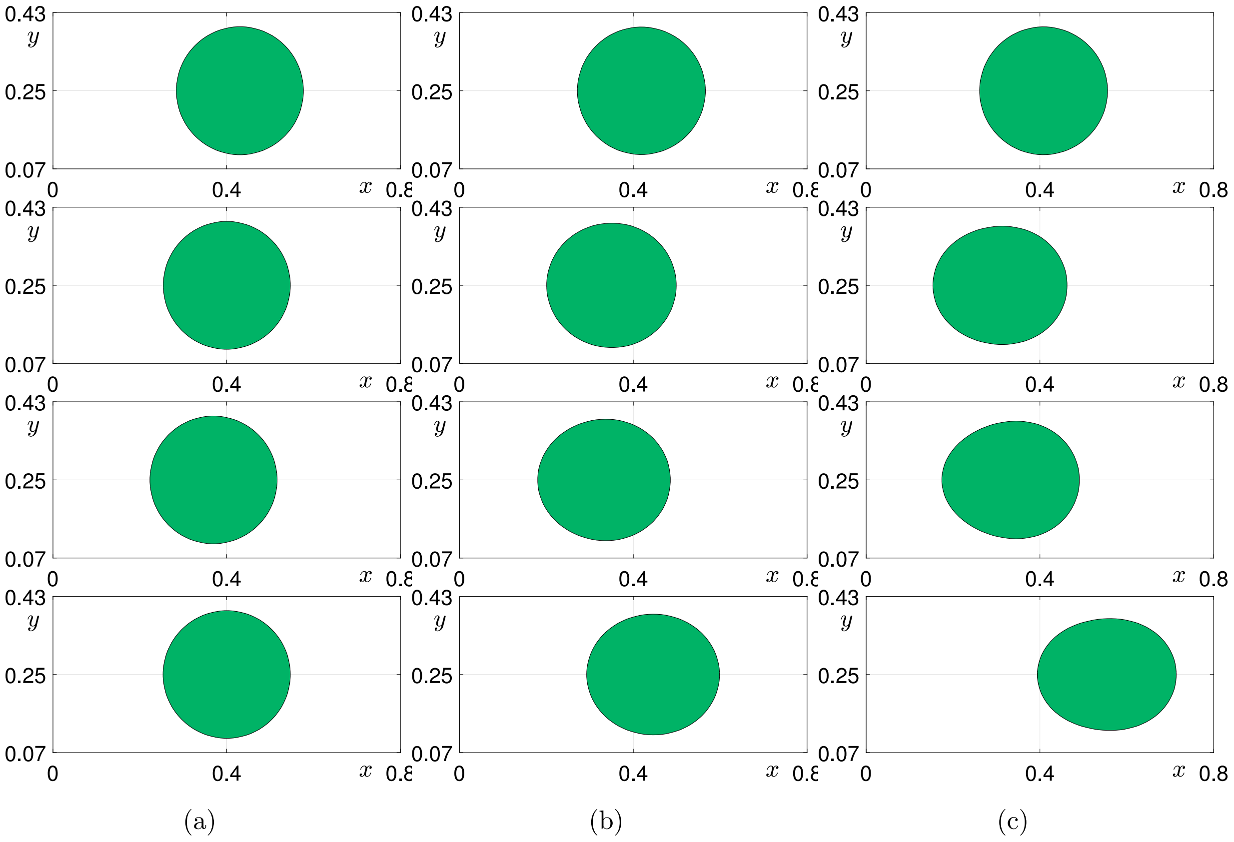

Fig. 8. Time evolutions of the filled contour at $t = 525\Delta t$, $t = 1050\Delta t$, $t = 1575\Delta t$, and $t = 2100\Delta t$ from the first to the fourth row, respectively. Each column corresponds to various values of the parameter (a) $\alpha = 1$, (b) $\alpha = 0.5$, and (c) $\alpha = 0.1$.

We use the following initial profile:

$$\phi(x, y, 0) = \tanh\left(\frac{0.2 - \sqrt{(x-0.5)^2 + (y-0.7)^2}}{\sqrt{2}\epsilon}\right)$$

on a unit domain. We use the parameters $h = 1/100$, $\epsilon = h$, and $\Delta t = h^2$.

Fig. 7 displays the evolution of the zero-level set of the computational solutions for $\alpha = 1$, $\alpha = 0.8$, and $\alpha = 0.5$. The contours for lower fractional orders ($\alpha = 0.5$ and $\alpha = 0.8$) show faster deformation and evolution compared to the classical case ($\alpha = 1$). This indicates that memory effects associated with fractional derivatives significantly accelerate phase evolution. As time progresses from $t = 1000\Delta t$, where the contours are relatively smooth with moderate deformation, to $t = 1500\Delta t$ and $t = 2000\Delta t$, where increasing complexity and noticeable deviations emerge based on the fractional order, the contours at $t = 3000\Delta t$ show the most pronounced deformation for $\alpha = 1$, while $\alpha = 0.5$ maintains a simpler circular shape. Lower values of α introduce stronger memory effects and lead to faster transitions. The influence of α becomes more obvious as time progresses, which highlights the role of fractional derivatives in governing the system's dynamics. This computational result effectively demonstrates how the fractional order parameter (α) influences the phase separation process. Smaller α values result in more dynamic and rapid changes, which emphasizes the use of fractional models for capturing temporal behaviors in phase-field equations with memory effects.

Next, let us consider the following time-periodic background flow in the x-direction over time, with no velocity component in the y-direction: $u(\mathbf{x}, t) = \cos(30t)$ and $v(\mathbf{x}, t) = 0$. We consider the following initial profile on $\Omega = (0, 0.8) \times (0, 0.5)$:

$$\phi(\mathbf{x}, 0) = \tanh\left(\frac{0.15 - \sqrt{(x-0.4)^2 + (y-0.25)^2}}{\sqrt{2}\epsilon}\right).$$

In the following test, we take numerical parameters as $h = 1/100$, $\epsilon = h$, and $\Delta t = h^2$. Fig. 8 shows the changes in the filled contour over time for various values of the parameter (a) $\alpha = 1$, (b) $\alpha = 0.5$, and (c) $\alpha = 0.1$.

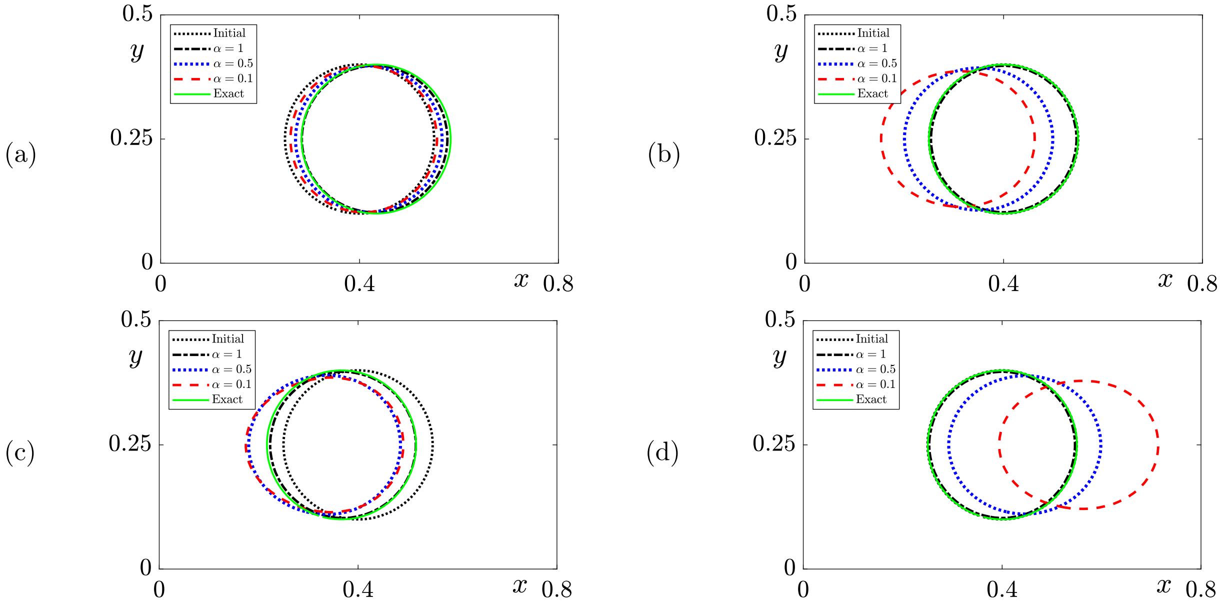

Fig. 9. Time evolution of the zero-level set of the computational solutions for $\alpha = 1$, $\alpha = 0.5$, and $\alpha = 0.1$ at (a) $t = 525\Delta t$, (b) $t = 1050\Delta t$, (c) $t = 1575\Delta t$, and (d) $t = 2100\Delta t$. (For interpretation of the references to color in this figure legend, the reader is referred to the web version of this article.)

Each row represents a specific time $t = 525\Delta t$, $t = 1050\Delta t$, $t = 1575\Delta t$, and $t = 2100\Delta t$, while each column shows the effect of varying α on the contour's shape. Because of the memory effect of time-fractional derivatives, the evolution over time increases as α decreases.

Fig. 9 illustrates the time evolution of the zero-level set of the computational solutions for $\alpha = 1$, $\alpha = 0.5$, and $\alpha = 0.1$. These results are compared with the reference profile derived from simple advection under the background flow at four time steps: (a) $t = 525\Delta t$, (b) $t = 1050\Delta t$, (c) $t = 1575\Delta t$, and (d) $t = 2100\Delta t$. The black dotted line represents the initial contour, while the blue, red, and magenta dashed lines correspond to numerical solutions for $\alpha = 1$, $\alpha = 0.5$, and $\alpha = 0.1$, respectively. The green solid line indicates the reference solution. For $\alpha = 1$, the numerical solution closely matches the reference solution across all time steps. For $\alpha = 0.5$, minor deviations appear and grow over time, which reflects a memory effect. In the case of $\alpha = 0.1$, substantial deviations from the reference solution occur, especially at later time steps, which indicates a significant memory effect. The time evolution of zero-level contours demonstrates that the computational results show varying degrees of deviation from the reference solution depending on the value of α. For $\alpha = 1$, the solutions agree with the reference profile, which indicates negligible memory effects. However, as α decreases, memory effects become increasingly significant, with $\alpha = 0.1$ showing substantial deviations, particularly at later time steps. This highlights the influence of α on the time evolution of the numerical solutions over time.

4. Conclusions

In this paper, we presented a normalized TFCH equation by incorporating time-fractional derivatives to more effectively account for memory effects in phase separation processes. By using a normalized time-fractional derivative, we were able to generalize the CH equation and capture complex temporal behaviors. To solve the normalized TFCH equation, we used an efficient Fourier spectral method, which provided high accuracy and computational efficiency. Our investigation into the dynamic behavior of the proposed model showed that the fractional-order time derivative plays a significant role in influencing the evolution of phase domains. Extensive numerical simulations demonstrated the capability of the normalized TFCH equation in accurately modeling phase separation dynamics over time. These numerical results confirm the versatility and robustness of our approach. In this paper, we numerically investigated the dynamics of the normalized TFCH equation; however, the well-posedness, stability, and uniqueness of solutions and mass conservation and energy dissipation properties of the normalized TFCH would require further investigation. And, the effect of the fractional parameter on the evolution speed of phase domains and the characteristic length scale of phase-separated regions also require further study. In future work, instead of considering the entire history, we will adopt the short-memory approach, which applies the short-memory principle to retain only a finite past interval [67,68]. This approach will improve computational efficiency and increase the calculation speed.

CRediT authorship contribution statement

Hyun Geun Lee: Writing – review & editing, Writing – original draft, Validation, Software, Resources, Methodology, Investigation, Formal analysis, Conceptualization. **Soobin Kwak:** Writing – review & editing, Writing – original draft, Visualization, Validation, Software, Data curation. **Seokjun Ham:** Writing – review & editing, Writing – original draft, Validation, Software, Investigation. **Youngjin Hwang:** Writing – review & editing, Writing – original draft, Visualization, Validation, Software, Investigation. **Junseok Kim:** Writing – review & editing, Writing – original draft, Supervision, Software, Resources, Project administration, Methodology, Funding acquisition, Formal analysis, Conceptualization.

Declaration of competing interest

The authors declare that they have no known competing financial interests or personal relationships that could have appeared to influence the work reported in this paper.

Acknowledgment

This work was supported by the Brain Korea 21 FOUR. We sincerely appreciate the constructive comments and valuable suggestions provided by the reviewers, which have significantly improved the quality of this manuscript.

Appendix

The following listing 1 is MATLAB code for the normalized TFCH equation.

Listing 1: MATLAB code for a normalized TFCH equation

```
clear all;
Nx = 100; Ny=50; Lx=0; Rx=2; Ly=0; Ry=1; h=(Rx–Lx)/Nx;
x=linspace(Lx+h/2,Rx–h/2,Nx); y=linspace(Ly+h/2,Ry–h/2,Ny);
dt = 100.0∗h^2; T=30; Nt = round(T/dt); dt=T/Nt;
v(1:Nx,1:Ny,1) = rand(Nx,Ny)−0.5;
k=2∗pi/(Rx–Lx)∗[0:Nx/2 –Nx/2+1:−1]; p=2∗pi/(Ry–Ly)∗[0:Ny/2 –Ny/2+1:−1];
k2=k.^2; p2=p.^2; [kk2, pp2]=meshgrid(k2,p2);
kp=kk2'+pp2'; kp2=kp.^2; t=0; eps2=1∗h^2;
u(:,:,1)=real(v);
flag=2;     % flag=1 is alpha=1
alp=0.5;
for n = 1:Nt
deno = n^(1−alp);
    for p = 1:n
        w(p) = ((n+1–p)^(1−alp)–(n–p)^(1−alp))/deno;
    end
    F = 0∗v;
    if n > 1
        for p = 1:n–1
            F = F+w(p)∗(u(:,:,p+1)–u(:,:,p))/dt;
        end
    end
    if flag==1
        w(n)=1;  F=0∗v;
    end
f=u(:,:,n).^3−3∗u(:,:,n);
v_hat = fft2(w(n)∗u(:,:,n)–dt∗F)–dt∗kp.∗fft2(f); %Converts to fourier space
v_hat = v_hat./(w(n)+dt∗(2.0∗kp+eps2∗kp2)); %Backwards Euler timestepping
u(:,:,n+1) = real(ifft2(v_hat)); %Converts back to real Space
t=t+dt;
if (mod(n,20)==0)
clf; surf(x,y,u(:,:,n+1)'); shading interp
axis([Lx Rx Ly Ry –1.1 1.1]); view(0,90); axis image; pause(0.01)
end
end
```

Data availability

No data was used for the research described in the article.

References

[1] Sadaf M, Akram G. Effects of fractional order derivative on the solution of time-fractional Cahn–Hilliard equation arising in digital image inpainting. Indian J Phys 2021;95:891–9. http://dx.doi.org/10.1007/s12648-020-01743-1.

[2] Zhao J, Chen L, Wang H. On power law scaling dynamics for time-fractional phase field models during coarsening. Commun Nonlinear Sci Numer Simul 2019;70:257–70. http://dx.doi.org/10.1016/j.cnsns.2018.10.019.

[3] Fritz M. Tumor evolution models of phase-field type with nonlocal effects and angiogenesis. Bull Math Biol 2023;85(6):44. http://dx.doi.org/10.1007/s11538-023-01151-6.

[4] Cahn JW, Hilliard JE. Free energy of a nonuniform system. I. Interfacial free energy. J Chem Phys 1958;28(2):258–67. http://dx.doi.org/10.1063/1.1744102.

[5] Cahn JW. On spinodal decomposition. Acta Metall 1961;9:795–801. http://dx.doi.org/10.1016/0001-6160(61)90182-1.

[6] Li Y, Liu R, Xia Q, He C, Li Z. An efficient numerical approach for multiphase flow problems. J Comput Appl Math 2022;401:113778. http://dx.doi.org/10.1016/j.cam.2021.113778.

[7] Yang J, Wang J, Tan Z, Kim J. A conservative phase-field method for multiphase systems. Comput Phys Comm 2023;282:108558. http://dx.doi.org/10.1016/j.cpc.2022.108558.

[8] Bae H. Global existence of unique weak solutions and decay rates of Active model B with the logarithmic Cahn–Hilliard equation in Wiener space. Chaos Solitons Fractals 2023;175:113922. http://dx.doi.org/10.1016/j.chaos.2023.113922.

[9] Kim J, Tan Z, Yang J. A robust numerical scheme for Allen–Cahn equations. Comput Math Appl 2023;143:133–50. http://dx.doi.org/10.1016/j.camwa.2023.05.002.

[10] Yang J, Li Y, Kim J. A numerical study of phase-field models for interfacial dynamics. J Comput Phys 2023;491:112345. http://dx.doi.org/10.1016/j.jcp.2023.112345.

[11] Xia Q, Liu Y, Kim J, Li Y. A thermal multiphase flow model with high accuracy. J Comput Appl Math 2023;433:115319. http://dx.doi.org/10.1016/j.cam.2023.115319.

[12] Xia Q, Yang J, Kim J, Li Y. A phase-field model for thermal multiphase flows. J Comput Phys 2024;513:113158. http://dx.doi.org/10.1016/j.jcp.2024.113158.

[13] Li Y, Qin K, Xia Q, Kim J. Numerical methods for complex flow problems. Appl Numer Math 2023;184:512–26. http://dx.doi.org/10.1016/j.apnum.2022.11.006.

[14] Xia B, Xi X, Yu R, Zhang P. An adaptive method for numerical simulations. Appl Numer Math 2024;198:192–201. http://dx.doi.org/10.1016/j.apnum.2024.01.005.

[15] Xie W, Feng J, Xia Q, Kim J, Li Y. Comput Methods Appl Mech Engrg 2024;429:117138. http://dx.doi.org/10.1016/j.cma.2024.117138.

[16] Xia Q, Sun G, Yu Q, Kim J, Li Y. Thermal-fluid topology optimization with unconditional energy stability and second-order accuracy via phase-field model. Commun Nonlinear Sci Numer Simul 2023;116:106782. http://dx.doi.org/10.1016/j.cnsns.2022.106782.

[17] Li Y, Lv Z, Xia Q. On the adaption of biological transport networks affected by complex domains. Phys Fluids 2024;36:101906. http://dx.doi.org/10.1063/5.0231079.

[18] Li Y, Wang J, Lu B, Jeong D, Kim J. Multicomponent volume reconstruction from slice data using a modified multicomponent Cahn–Hilliard system. Pattern Recognit 2019;93:124–33. http://dx.doi.org/10.1016/j.patcog.2019.04.006.

[19] Li J, Yang J. Local volume-conservation-improved diffuse interface model for simulation of Rayleigh–Plateau fluid instability. Comput Phys Comm 2024;296:109050. http://dx.doi.org/10.1016/j.cpc.2023.109050.

[20] Zheng R, Jiang X. Spectral methods for the time-fractional Navier–Stokes equation. Appl Math Lett 2019;91:194–200. http://dx.doi.org/10.1016/j.aml.2018.12.018.

[21] Fritz M, Rajendran ML, Wohlmuth B. Time-fractional Cahn–Hilliard equation: Well-posedness, degeneracy, and numerical solutions. Comput Math Appl 2022;108:66–87. http://dx.doi.org/10.1016/j.camwa.2022.01.002.

[22] Marks RJ, Hall MW. Differintegral interpolation from a bandlimited signal's samples. IEEE Trans Signal Process 1981;29:872–7. http://dx.doi.org/10.1109/TASSP.1981.1163636.

[23] Diethelm K, Freed AD. On the solution of nonlinear fractional-order differential equations used in the modeling of viscoplasticity. In: Scientific computing in chemical engineering II. Berlin, Heidelberg: Springer Berlin Heidelberg; 1999, p. 217–24. http://dx.doi.org/10.1007/978-3-642-60185-9_24.

[24] Bosch J, Stoll M. A fractional inpainting model based on the vector-valued Cahn–Hilliard equation. SIAM J Imaging Sci 2015;8:2352–82. http://dx.doi.org/10.1137/15M101405X.

[25] Koeller RC. Applications of fractional calculus to the theory of viscoelasticity. J Appl Mech 1984;51(2):299–307. http://dx.doi.org/10.1115/1.3167616.

[26] Mainardi F. Fractional calculus and waves in linear viscoelasticity: An introduction to mathematical models. World Scientific 2022. http://dx.doi.org/10.1142/p926.

[27] Ren J, Lei H, Song J. An improved lattice Boltzmann model for variable-order time-fractional generalized Navier–Stokes equations with applications to permeability prediction. Chaos Solitons Fractals 2024;189:115616. http://dx.doi.org/10.1016/j.chaos.2024.115616.

[28] Torvik PJ, Bagley RL. On the appearance of the fractional derivative in the behavior of real materials. J Appl Mech 1984;51:294–8. http://dx.doi.org/10.1115/1.3167615.

[29] Oskouie MF, Ansari R, Rouhi H. Bending analysis of functionally graded nanobeams based on the fractional nonlocal continuum theory by the variational Legendre spectral collocation method. Meccanica 2018;53:1115–30. http://dx.doi.org/10.1007/s11012-017-0792-0.

[30] Sumelka W, Blaszczyk T, Liebold C. Fractional Euler–Bernoulli beams: Theory, numerical study and experimental validation. Eur J Mech A- Solids 2015;54:243–51. http://dx.doi.org/10.1016/j.euromechsol.2015.07.002.

[31] Lazopoulos KA, Lazopoulos AK. On fractional bending of beams. Arch Appl Mech 2016;86(6):1133–45. http://dx.doi.org/10.1007/s00419-015-1083-7.

[32] Lazopoulos KA, Lazopoulos AK. On the fractional deformation of a linearly elastic bar. J Mech Behav Mater 2020;29(1):9–18. http://dx.doi.org/10.1515/jmbm-2020-0002.

[33] Sidhardh S, Patnaik S, Semperlotti F. Geometrically nonlinear response of a fractional-order nonlocal model of elasticity. Int J Non-Linear Mech 2020;125:103529. http://dx.doi.org/10.1016/j.ijnonlinmec.2020.103529.

[34] Stempin P, Sumelka W. Space-fractional Euler–Bernoulli beam model-theory and identification for silver nanobeam bending. Int J Mech Sci 2020;186:105902. http://dx.doi.org/10.1016/j.ijmecsci.2020.105902.

[35] Liu H, Cheng A, Wang H, Zhao J. Time-fractional Allen–Cahn and Cahn–Hilliard phase-field models and their numerical investigation. Comput Math Appl 2018;76:1876–92. http://dx.doi.org/10.1016/j.camwa.2018.07.036.

[36] Tang T, Yu H, Zhou T. On energy dissipation theory and numerical stability for time-fractional phase-field equations. SIAM J Sci Comput 2019;41:A3757–78. http://dx.doi.org/10.1137/18M1203560.

[37] Saleh R, Kassem M, Chin Mabrouk SM. Exact solutions of nonlinear fractional order partial differential equations via singular manifold method. J Phys 2019;61:290–300. http://dx.doi.org/10.1016/j.cjph.2019.09.005.

[38] Ye H, Liu Q, Chen ZM. Global existence of solutions of the time fractional Cahn–Hilliard equation in $\mathbb{R}^3$. J Evol Equ 2021;21:2377–411. http://dx.doi.org/10.1007/s00028-021-00687-1.

[39] Liao HL, Liu N, Zhao X. Asymptotically compatible energy of variable-step fractional BDF2 scheme for the time-fractional Cahn–Hilliard model. IMA J Numer Anal 2024;drae034. http://dx.doi.org/10.1093/imanum/drae034.

[40] Zhang J, Zhao J, Wang J. A non-uniform time-stepping convex splitting scheme for the time-fractional Cahn–Hilliard equation. Comput Math Appl 2020;80:837–50. http://dx.doi.org/10.1016/j.camwa.2020.04.031.

[41] Liu Z, Li X, Huang J. Accurate and efficient algorithms with unconditional energy stability for the time fractional Cahn–Hilliard and Allen–Cahn equations. Numer Meth Part Differ Equ 2021;37:2613–33. http://dx.doi.org/10.1002/num.22752.

[42] Ran M, Zhou X. An implicit difference scheme for the time-fractional Cahn–Hilliard equations. Math Comput Simulation 2021;180:61–71. http://dx.doi.org/10.1016/j.matcom.2020.08.021.

[43] Tang T, Wang B, Yang J. Asymptotic analysis on the sharp interface limit of the time-fractional Cahn–Hilliard equation. SIAM J Appl Math 2022;82:773–92. http://dx.doi.org/10.1137/21M1427863.

[44] Chen L, Lü S. A fully discrete spectral scheme for time fractional Cahn-Hilliard equation with initial singularity. Comput Math Appl 2022;127:213–24. http://dx.doi.org/10.1016/j.camwa.2022.10.015.

[45] Huang C, An N, Yu X. Unconditional energy dissipation law and optimal error estimate of fast L1 schemes for a time-fractional Cahn–Hilliard problem. Commun Nonlinear Sci Numer Simul 2023;124:107300. http://dx.doi.org/10.1016/j.cnsns.2023.107300.

[46] Zhang H, Jiang X. A high-efficiency second-order numerical scheme for time-fractional phase field models by using extended SAV method. Nonlinear Dynam 2020;102(1):589–603. http://dx.doi.org/10.1007/s11071-020-05943-6.

[47] Quan C, Tang T, Yang J. How to define dissipation-preserving energy for time-fractional phase-field equations. CSIAM Trans Appl Math 2020;1(3):478–90. http://dx.doi.org/10.4208/csiam-am.2020-0024.

[48] Quan C, Tang T, Yang J. Numerical energy dissipation for time-fractional phase-field equations. CSIAM Trans Appl Math 2025;43(3):515–39. http://dx.doi.org/10.4208/jcm.2311-m2021-0199.

[49] Quan C, Wang B. Energy stable L2 schemes for time-fractional phase-field equations. J Comput Phys 2022;458:111085. http://dx.doi.org/10.1016/j.jcp.2022.111085.

[50] Yu Y, Zhang J, Qin R. The exponential SAV approach for the time-fractional Allen–Cahn and Cahn–Hilliard phase-field models. J Sci Comput 2023;94:33. http://dx.doi.org/10.1007/s10915-022-02085-2.

[51] Karaa S. Positivity of discrete time-fractional operators with applications to phase-field equations. SIAM J Numer Anal 2021;59(4):2040–53. http://dx.doi.org/10.1137/20M1368641.

[52] Al-Maskari M, Karaa S. The time-fractional Cahn–Hilliard equation: analysis and approximation. IMA J Numer Anal 2022;42:1831–65. http://dx.doi.org/10.1093/imanum/drab025.

[53] Guo W, Zhen Y, Jiang T. An efficient pure meshless method for phase separation dominated by time-fractional Cahn–Hilliard equations. Int J Model Simul Sci Comput 2024;15:2450012. http://dx.doi.org/10.1142/S1793962324500120.

[54] Liang H, Zhang C, Du R, Wei Y. Lattice Boltzmann method for fractional Cahn–Hilliard equation. Commun Nonlinear Sci Numer Simul 2020;91:105443. http://dx.doi.org/10.1016/j.cnsns.2020.105443.

[55] Khristenko U, Wohlmuth B. Solving time-fractional differential equations via rational approximation. IMA J Numer Anal 2023;43:1263–90. http://dx.doi.org/10.1093/imanum/drac022.

[56] Qi RJ, Zhang W, Zhao X. Variable-step numerical schemes and energy dissipation laws for time fractional Cahn–Hilliard model. Appl Math Lett 2024;149:108929. http://dx.doi.org/10.1016/j.aml.2023.108929.

[57] Zhang H, Liao HL. High-order energy stable variable-step schemes for the time-fractional Cahn–Hilliard model. Math Comput Simulation 2024;223:171–82. http://dx.doi.org/10.1016/j.matcom.2024.04.005.

[58] Kawarkhe AV, Avhale PS, Magar V. Reduced differential transform method for fractional order partial differential equations. J Comput Anal Appl 2024;33(6):1051–5, Available from: http://www.eudoxuspress.com/index.php/pub/article/view/980.

[59] Hassan A, Arafa AAM, Rida SZ, Dagher MA, El Sherbiny HM. Adapting semi-analytical treatments to the time-fractional derivative Gardner and Cahn–Hilliard equations. Alex Eng J 2024;87:389–97. http://dx.doi.org/10.1016/j.aej.2023.12.056.

[60] Lee C, Nam Y, Bang M, Ham S, Kim J. Numerical investigation of the dynamics for a normalized time-fractional diffusion equation. AIMS Math 2024;9:26671–87. http://dx.doi.org/10.3934/math.20241297.

[61] Jornet M, Nieto JJ. Power-series solution of the L-fractional logistic equation. Appl Math Lett 2024;154:109085. http://dx.doi.org/10.1016/j.aml.2024.109085.

[62] Lazopoulos KA, Lazopoulos AK. Fractional vector calculus and fractional continuum mechanics. Progr Fract Differ Appl 2016;2:67–86. http://dx.doi.org/10.18576/pfda/020202.

[63] Calatayud J, Jornet M, Pinto CM. On the interpretation of Caputo fractional compartmental models. Chaos Solitons Fractals 2024;186:115263. http://dx.doi.org/10.1016/j.chaos.2024.115263.

[64] Hammad HA, Alshehri MG. Application of the Mittag-Leffler kernel in stochastic differential systems for approximating the controllability of nonlocal fractional derivatives. Chaos Solitons Fractals 2024;182:114775. http://dx.doi.org/10.1016/j.chaos.2024.114775.

[65] Yoon S, Jeong D, Lee C, Kim H, Kim S, Lee HG, Kim J. Fourier-spectral method for the phase-field equations. Mathematics 2020;8:1385. http://dx.doi.org/10.3390/math8081385.

[66] Yang J, Li Y, Kim J. Phase-field modeling and linearly energy-stable Runge–Kutta algorithm of colloidal crystals on curved surfaces. J Comput Appl Math 2024;443:115750. http://dx.doi.org/10.1016/j.cam.2023.115750.

[67] Zhou Y, Zhang Y. Noether symmetries for fractional generalized Birkhoffian systems in terms of classical and combined Caputo derivatives. Acta Mech 2020;231(7):3017–29. http://dx.doi.org/10.1007/s00707-020-02690-y.

[68] Malendowski M, Sumelka W, Gajewski T, Studziński R, Peksa P, Sielicki PW. Prediction of high-speed debris motion in the framework of time-fractional model: theory and validation. Arch Civ Mech Eng 2022;23(1):46. http://dx.doi.org/10.1007/s43452-022-00568-5.